# Design and Test Analysis of a Solar Array Root Hinge Drive Assembly

DING Xilun and LI Xin*

*Robotics Institute, Beihang University, Beijing 100191, China*

**Abstract:** A root hinge drive assembly is preferred in place of the classical viscous damper in a large solar array system. It has advantages including better deployment control and higher reliability. But the traditional single degree of freedom model should be improved. A multiple degrees of freedom dynamics model is presented for the solar arrays deployment to guide the drive assembly design. The established model includes the functions of the torsion springs, the synchronization mechanism and the lock-up impact. A numerical computation method is proposed to solve the dynamics coupling problem. Then considering the drive torque requirement calculated by the proposed model, a root hinge drive assembly is developed based on the reliability engineering design methods, and dual actuators are used as a redundancy design. Pseudo-efficiency is introduced and the major factors influencing the (pseudo-) efficiency of the gear mechanism designed with high reduction ratio are studied for further test data analysis. A ground prototype deployment test is conducted to verify the capacity of the drive assembly. The test device consists of a large-area solar array system and a root hinge drive assembly. The RHDA development time is about 43 s. The theoretical drive torque is compared with the test values which are obtained according to the current data and the reduction efficiency analysis, and the results show that the presented model and the calibration methods are proper enough.

**Keywords:** solar array, root hinge drive assembly, dynamics model, transmission efficiency, redundancy design, reliability

## 1 Introduction

Most of the spacecraft electrical power is provided by solar arrays. Rigid multi-panel arrays are folded in a stowed configuration before being launched. In an on-orbit state, the solar arrays are allowed to deploy under their joints elastic strain energy[1–3], but the deployment velocities are difficult to regulate. The solar array panels need to be locked when they are fully deployed. The locking impact may disturb the spacecraft flight or even destroy the structure. To decrease the deployment velocity, normally, a rotary viscous damper assembly is employed, mounting to the root hinge where the yoke is connected to the spacecraft[4–6]. The increasing requirements of electric power have led to the need to use large-area and multi-stage deployable arrays[7–9], but such arrays cause more serious impact. In this situation, the viscous damper has a limit effect. HWANG[10] pointed that it was a quite challenging task to define the deployment scheme for the huge solar array's successful deployment. The problem has motivated an interest in motorized mechanical designs in place of the damper assembly to control the deployment velocity. For example, the array joints driven by motors

were studied by PORRO, et al[11].

The multi-panel arrays deployment synchronization is approximately realized by using a CCL(closed cable loop) system. The deployment can be seen as a single-DOF motion which makes its relevant analysis simple and convenient. LI, et al[12], and BAI, et al[13], studied the effect of the CCL on the dynamic performance of deployable mechanisms. The synchronization may be disturbed by introducing a damper or a root hinge drive assembly (RHDA), and it brings great differences between the actual test and the simplified model. KWAK, et al[14] addressed a multi-DOF model for a solar array system with strain energy hinges, but it did not involve drive assembly and root hinge torque. A more reasonable model is needed to analyze the output torque of the RHDA. Moreover, since the aerospace mechanism puts forward higher reliability requirements, it is necessary to adopt more effective methods for the RHDA design. Such as the redundancy design method which is also widely applied in nuclear energy and equipment manufacturing area[15].

This paper establishes a multi-degree dynamics model considering the RHDA effect and presents a detailed process for computing the root hinge drive torque. Then based on the reliability design methods, a RHDA with dual actuators and reduction devices was developed for a large deployable solar array system. By the ground prototype tests, the velocity and current of the actuators were recorded. It is not convenient to measure the drive torque

directly because of the dimensional limits. But for a DC motor, its mechanical torque is proportional to the electrical current. Taking more factors like the reduction ratio and transmission efficiency into consideration, the output torque of the designed assembly can be known. So another study investigated the transmission efficiency varying performance of the RHDA. The effects of the RHDA were verified by the ground tests and the torque analysis results were used to validate the presented model.

## 2　Dynamics Model

The torque of the root hinge during the deployment is a crucial criterion for the RHDA component selections. The analysis is as follows.

A typical multi-panel solar array system is shown in Fig. 1. The system consists of a yoke and five panels, and all of them are folded during the stowed and ascent states. The deployment is divided into two stages. During the primary stage, only the outmost panel is released and turns ninety degrees. The secondary stage frees all panels and is the principal deployment, and Fig. 1 shows the process.
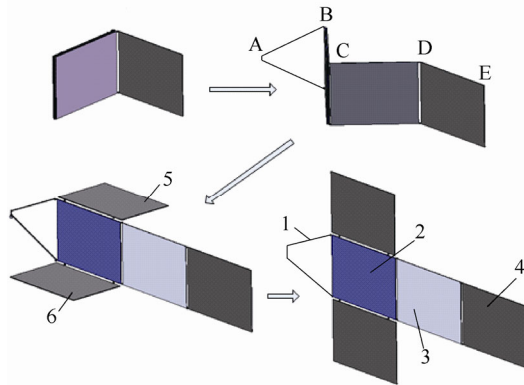


Fig. 1.　Deployment of solar arrays

In Fig. 1, the yoke 1 and all the panels are driven by the RHDA and torsion springs. Panel 5 and panel 6 start to move synchronously after panel 2 and panel 3 are fully deployed, and they have less influence on the RHDA. Therefore, according to the secondary stage, a dynamics model is established in Fig. 2, considering the factors which are closely related to the root hinge drive torque[16].
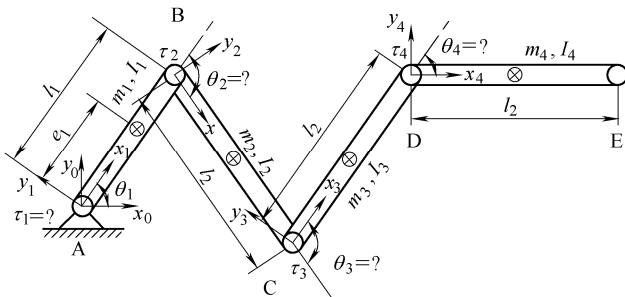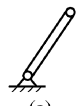


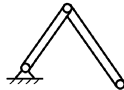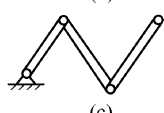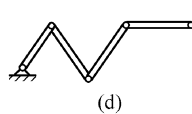Fig. 2.　Solar arrays secondary deployment model

In Fig. 2, assuming all links are rigid bodies, AB is the

yoke 1, and A is the root hinge. Joints B, C and D are acted upon by torsion spring torques. BC represents panels 2, 5 and 6 together; CD, DE are panel 3 and panel 4, respectively. All links are the same with length $l_2$ and homogeneous in density except link AB, and their masses are shown in the figure. Frame {0} is a fixed coordinate system; other frames are affixed to the corresponding links.

The deployment synchronization is provided approximately by a synchronization system. The system is comprised of several pulleys mounted to the hinges and a series of steel cables keyed to these pulleys. The cables have similar behaviors to the synchronous belts but with adjustable spring assemblies in the closed cable loops[17]. The pulley radiuses are different because their deployment angular displacements are not the same. When an adjacent panels' asynchronous phenomenon happens, an extra torque is caused by the changed cable tension to try to eliminate it.

In consideration of this influence, several studies addressed single-DOF deployment models[18], and their motion analytical results are satisfied enough. However, some problems emerge as the models are used to analyze the root hinge torque. Take the arrays in Fig. 2 as an example, if a RHDA are used to control the root hinge with a constant velocity, according to the single-DOF model, all the other panels will move with stable velocities. Then the root hinge drive torques for some cases are listed in Table 1 (the variables and frames are the same as shown in Fig. 2).

Table 1.　Root hinge drive torque of single-DOF model

| Case | Torque |
|---|---|
| (a) | $\tau_1^{(a)} = 0$ |
| (b) | $\tau_1^{(b)} = h_{12}^{(b)}\dot{\theta}_1\dot{\theta}_2 + h_{22}^{(b)}\dot{\theta}_2^2 = 0$ |
| (c) | $\tau_1^{(c)} = h_{12}^{(c)}\dot{\theta}_1\dot{\theta}_2 + h_{13}^{(c)}\dot{\theta}_1\dot{\theta}_3 + h_{22}^{(c)}\dot{\theta}_2^2 + h_{23}^{(c)}\dot{\theta}_2\dot{\theta}_3 + h_{33}^{(c)}\dot{\theta}_3^2 = 0$ |
| (d) | $\tau_1^{(d)} = h_{12}^{(d)}\dot{\theta}_1\dot{\theta}_2 + h_{13}^{(d)}\dot{\theta}_1\dot{\theta}_3 + h_{14}^{(d)}\dot{\theta}_1\dot{\theta}_4 + h_{22}^{(d)}\dot{\theta}_2^2 + h_{23}^{(d)}\dot{\theta}_2\dot{\theta}_3 + h_{24}^{(d)}\dot{\theta}_2\dot{\theta}_4 + h_{33}^{(d)}\dot{\theta}_3^2 + h_{34}^{(d)}\dot{\theta}_3\dot{\theta}_4 + h_{44}^{(d)}\dot{\theta}_4^2 = -m_4l_1l_2\sin\theta_1\dot{\theta}_1^2 / 2$ |

In case (a), there is only one yoke, and other cases are constructed in succession according to Fig. 2. In Table 1, $h_{ij}$ are coefficients about mass and length. In case (b) and case (c), we have $\left|\dot{\theta}_2\right| = \left|\dot{\theta}_3\right| = 2\left|\dot{\theta}_1\right|$, and both of the computed torque results are 0 N·m. For example, in case (b), $\left|h_{12}^{(b)}\right| = -m_2l_1l_2\sin\theta_2$ and $\left|h_{22}^{(b)}\right| = -1/2m_2l_1l_2\sin\theta_2$, so $\tau_1^{(b)} = 0$. In fact, if cases continue being constructed as case (b) and case (c) (excluding case (d)), the results are still 0 and they are independent of mass and length.

In fact, the synchronization may be disturbed by using the RHDA. Large solar arrays with longer arms of forces and greater masses will have significant effects on the root hinge. So there are remarkable errors in the mentioned single-DOF model. The joint accelerations and lock-up impact functions are not considered into the studied multi-DOF model either. To solve these problems, a dynamics analysis is presented as follows.

In Fig. 2, the joint torque at B(and C, D) consists of a torsion spring torque $\tau_i^s$ and an extra torque $\tau_i^c$ exerted by the synchronization mechanism. At joint A, the RHDA drive torque $\tau_A$ should also be considered. So the joint torque $\tau_i$ can be expressed as

$$\tau_i = \begin{cases} \tau_A + \tau_i^s + \tau_i^c, & i = 1, \\ \tau_i^s + \tau_i^c, & i \geqslant 2. \end{cases} \quad (1)$$

The torsion spring torque is linearly related to the spring twisting angle. Considering the damping effect, the torque is given by

$$\tau_i^s = \tau_i^{pre} - k_i^s \theta_i - c_i \dot{\theta}_i, \quad (2)$$

where $k_i^s$ and $c_i$ $(i=1, 2, \cdots)$ are the coefficients of stiffness and damping for torsion spring $i$, and $\tau_i^{pre}$ denotes the preload torque. These coefficients can be modified according to the ground test performance, to compensate the air resistance influence. The previous study showed the method in Ref. [16].

The initial angular positions $\theta_i(0)$ of the four joints are 90°, −180°, 180° and −90°, respectively, and all with terminal angles 0°. According to the angle information, the pulley radiuses proportion is determined, and the extra torque can be written as

$$\tau_i^c = k_{i-1}^c \left( \left\| \frac{\theta_i(0)}{\theta_{i-1}(0)} \right\| \theta_{i-1} + \theta_i \right) - k_i^c \left( \left\| \frac{\theta_{i+1}(0)}{\theta_i(0)} \right\| \theta_i + \theta_{i+1} \right), \quad (3)$$

where $k_i^c$ $(i=1, 2, \cdots)$ denotes the relevant coefficient of the synchronization system. Other drag forces can be represented by modifying these mentioned parameters. The drive torque of the RHDA $\tau_A$ can be given from Eq. (1).

In the space environment, i.e. no gravity or air resistance exists, so the dynamic equation is

$$\tau = M(\Theta)\ddot{\Theta} + V(\Theta, \dot{\Theta}), \quad (4)$$

where $\tau = [\tau_1, \tau_2, \tau_3, \tau_4]^T$ is a vector of the joint torque; $\ddot{\Theta} = [\ddot{\theta}_1, \ddot{\theta}_2, \ddot{\theta}_3, \ddot{\theta}_4]^T$ is a vector of the joint accelerations; $M(\Theta)$ is a mass matrix of the solar array system, and $V(\Theta, \dot{\Theta})$ is a vector of centrifugal and Coriolis terms.

The angular accelerations can be solved from Eq. (4) as

$$\ddot{\Theta} = M^{-1}(\Theta)[\tau - V(\Theta, \dot{\Theta})]. \quad (5)$$

Not all the velocity or torque values are known, so Eqs. (4) and (5) are both needed to get a simultaneous solution including the drive torque expression. The joint torques are directly affected by the panel angular velocities and accelerations; while the panel angular accelerations are determined by the joint drive forces. To solve $\tau_A$, this coupling problem of dynamics and inverse dynamics should be considered, so a numerical method is proposed as shown in Fig. 3. The relevant variables are renewed with time.
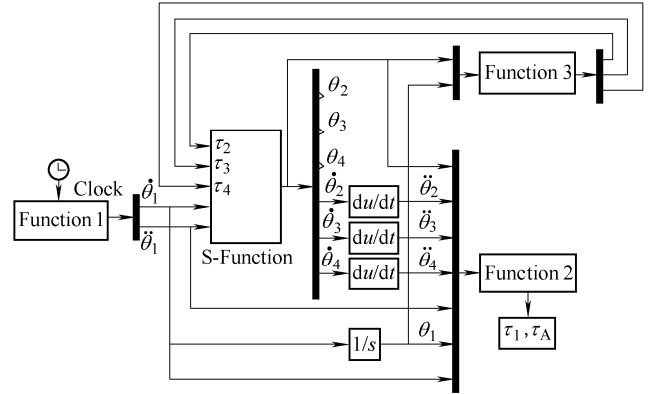


Fig. 3. Solution schematic diagram

In Fig. 3, Function 1 is used to provide the RHDA angular velocity $\dot{\theta}_1$ and angular acceleration $\ddot{\theta}_1$. $\dot{\theta}_1$ and $\ddot{\theta}_1$ are as the input parameters for S-Function with the known $\tau_2(0)$, $\tau_3(0)$ and $\tau_3(0)$(the initial torsion spring forces are known, and with no extra torque). In S-Function, the angular accelerations are computed according to Eq. (5), with output angular velocities and positions. In Function 2, the root hinge torque is calculated by using Eq. (1) and Eq. (4). Simultaneously, the torsion spring torque values are updated from these new positions and velocities information, by using Eq. (1), Eq. (2) and Eq. (3) together in Function 3. During the process, if any array deployment angle reaches the terminal value, another torque is exerted to simulate the lock-up impact. $M(\Theta)$ and $V(\Theta, \dot{\Theta})$ are needed in S-Function and Function 2 can be solved based on the Newton-Euler dynamics algorithm, let

$$_{i+1}^i R = \begin{pmatrix} \cos\theta_{i+1} & -\sin\theta_{i+1} & 0 \\ \sin\theta_{i+1} & \cos\theta_{i+1} & 0 \\ 0 & 0 & 1 \end{pmatrix}. \quad (6)$$

First, inertial forces are computed from yoke 1 to panel 4 iteratively[19–20]:

$$\begin{cases} {}^{i+1}\dot{v}_{i+1} = {}_{i+1}^i R^T \left\{ {}^i\dot{v}_i + \left[ -l_i \left( \sum_{j=1}^{i} \dot{\theta}_j \right)^2, l_i \sum_{j=1}^{i} \ddot{\theta}_j, 0 \right]^T \right\}, \\ {}^{i+1}\dot{v}_{i+1}^c = {}^{i+1}\dot{v}_{i+1} + \left[ -e_{i+1} \left( \sum_{j=1}^{i+1} \dot{\theta}_j \right)^2, e_{i+1} \sum_{j=1}^{i+1} \ddot{\theta}_j, 0 \right]^T, \\ {}^{i+1}F_{i+1} = m_{i+1} {}^{i+1}\dot{v}_{i+1}^c, \\ {}^{i+1}N_{i+1} = \left( 0, 0, I_{i+1} \sum_{j=1}^{i+1} \ddot{\theta}_j \right)^T, \end{cases} \quad (7)$$

where ${}^{i}\dot{\boldsymbol{v}}_{i}$ and ${}^{i}\dot{\boldsymbol{v}}_{i}^{c}$ are the $i$th acceleration of origin and center of mass with respect to frame $\{i\}$, respectively; $m_i$ and $I_i$ are the mass and moment of inertia panel $i$; ${}^{i}\boldsymbol{F}_{i}$ is the force acting at the center of the mass and ${}^{i}\boldsymbol{N}_{i}$ is the moment acting on the panel. Offset value of center of mass $e_i$ can be expressed as

$$e_i = \begin{cases} e_1, & i=1, \\ 0.5l_i, & i \geqslant 2. \end{cases} \tag{8}$$

Then, the interaction forces and torques and the joint torques are computed recursively back:

$$\begin{cases} {}^{i}\boldsymbol{f}_{i} = {}_{i+1}^{i}\boldsymbol{R}^{i+1}\boldsymbol{f}_{i+1} + {}^{i}\boldsymbol{F}_{i}, \\ {}^{i}\boldsymbol{n}_{i} = {}^{i}\boldsymbol{N}_{i} + {}_{i+1}^{i}\boldsymbol{R}^{i+1}\boldsymbol{n}_{i+1} + (e_i,0,0)^{\mathrm{T}} \times {}^{i}\boldsymbol{F}_{i} + \\ \qquad (l_i,0,0)^{\mathrm{T}} \times {}_{i+1}^{i}\boldsymbol{R}^{i+1}\boldsymbol{f}_{i+1}, \\ \tau_i = (0,0,1) {}^{i}\boldsymbol{n}_{i}, \end{cases} \tag{9}$$

where ${}^{i}\boldsymbol{f}_{i}$ is the force exerted on panel $i$, and ${}^{i}\boldsymbol{n}_{i}$ is the torque exerted on panel $i$.

The results are listed in Appendix.

# 3 Design of the RHDA

The above analysis is an important basis for the RHDA components design. Besides, there are special design requirements of a spacecraft mechanism, and the primary function of a RHDA is to deploy the arrays reliably. Based on the reliability design, and the specifications of the drive assembly, several reliability design methods, such as preventive design, fundamental design, margin design and redundancy design can be used.

## 3.1 Preventive design

The weak links in the product design can be pointed out by preventive design process. The drive principle is that the planetary gear unit is driven by a motor after being slowed down by a rotary gear train to provide low speed and high torque output. Based on fault tree analysis(FTA) which is a method of preventive design, it is found that the motor has a largest failure probability, so the motor can be designed by using redundancy design method. Failure of the gear shafts and the planetary gear unit is primarily caused by bending stress, so the gear train can be designed by using margin design method.

## 3.2 Fundamental design and margin design

The overall design of the RHDA consists of four main components: motor, planetary gear unit, gear shafts and torque limiter. The transmission principle is as shown in Fig. 4, and the output side of the planetary gear unit is connected to the root hinge.
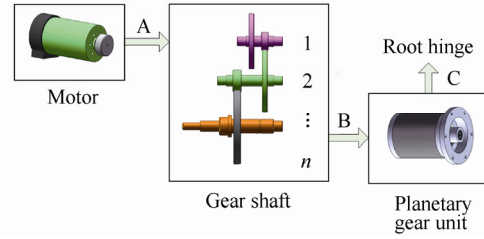


Fig. 4. Schematic diagram of transmission principle

In space environment, low power DC motors are preferred. To fulfill the output speed and torque requirements, gear shafts and planetary gear unit were used as shown in the diagram, and the torque was calculated from Fig. 3. Considering air resistance and suspension system drags, they can be transferred to joint effects based on previous test data. This method by modifying joint parameters ensured the deployment closed to the actual behaviors.

The reliable structure of the gear shafts can be ensured by using margin design method. Some margin design standards are summarized in Table 2[21] as a reference.

**Table 2. Part of standard of margin design**

| Item | Margin of safety(statics moment) $MOS_{sm}$ | Margin of safety (dynamics moment) $MOS_{dm}$ |
|---|---|---|
| US Military Standard MIL-HDBK-83577 | $100\left(\dfrac{M_d - M_{nd}}{M_r} - 1\right) \geqslant \beta$ $\beta = \begin{cases} 1.75 & \text{Draft} \\ 1.50 & \text{Preliminary} \\ 1.25 & \text{Prototype} \\ 1.00 & \text{Final} \end{cases}$ | $100\left(\dfrac{M_d - M_r}{M_{nd}} - 1\right) \geqslant 0.25$ |
| ESA Standard ECSS-E-30 | $\dfrac{M_d}{M_r} \geqslant 2$ | $\dfrac{M_d - 2M_r}{M_i} \geqslant 1.25$ |
| National Military Standard of China GJB 4038-2000 | Solar array deployment mechanism: $\dfrac{M_d}{M_r} - 1 \geqslant 1$ | — |

In Table 2, $M_d$ and $M_r$ are drive moment and resisting moment respectively; $M_{nd}$ and $M_i$ are drive and inertia moment caused by acceleration.

According to the RHDA drive torque calculation, a planetary gear unit was selected, and a set of reduction ratios for the gear shafts were assigned. Then the gear shaft $n$ has the maximum load. In this special case, the gears work in a medium speed and plume load condition. So 40Cr after quenching and tempering treatment was used. The minimum diameter of the gear shaft is 5 mm in accordance with Table 2 and the structure requirements.

The gear shafts designed by margin design method can bear a higher load, but the motor might be blocked and

destroyed, thus, a torque limiter should be introduced to protect the motor when the system overloads for a long time. The torque limiter will disengage then become in a protection state if the exterior torque goes too high, and it can revert to the original state automatically. The states are detected by a proximity switch. As shown in Fig. 4, because the disengaging torque is rather low at position A, so the limiter is difficult to design. Position C is also not suitable for a limiter's installation, as the limiter at position C will be much bigger and heavier compared with that at the optimum position B.

### 3.3 Redundancy design

According to the preventive analysis, the most important component of the RHDA is the motor but it has the highest probability of failure, so redundancy power inputs should be applied. In the view of reliability optimization, and further of meeting the limits of weight, size and cost, using two motors is the best choice for the configuration. Therefore, the transmission is improved as shown in Fig. 5.
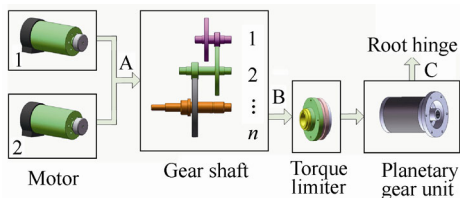


Fig. 5.    Schematic diagram of modified transmission principle

In a normal running situation, motor 1 drives the gear train and motor 2 follows. The torque limiter transmits the rotary motion to the gear shaft $n$ which turns the planetary gear unit. If the limiter overloads, a sliding between the two parts of the limiter will occur to protect the gear shafts and the motors. Once motor 1 is failure, motor 2 will be put into the working order instantly. The dual motors also support collaborative work mode if they are set properly.

A solid graphic model of this RHDA is established in the following, as shown in Fig. 6.
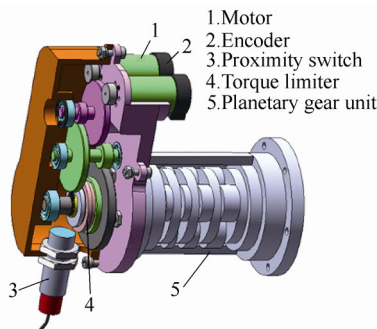


Fig. 6.    Design draft of the RHDA

## 4    Ground Tests and Analysis

To validate the functions of the RHDA on the solar arrays, ground tests were conducted. For the large multiple-stage packaging and deployable solar array system designed by *China Academy of Space Technology*, a RHDA (see Fig. 7) was developed with its test control cabinet.
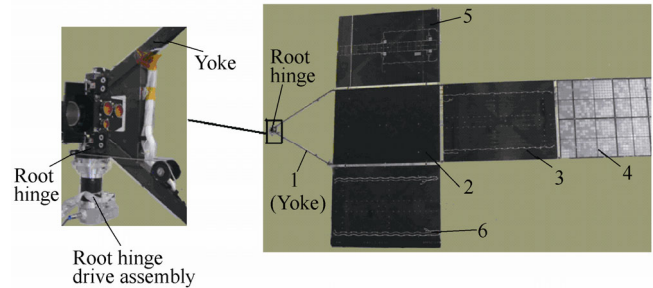


Fig. 7.    Solar array test platform

Finally, the determined control strategy of the RHDA is that motor 1 drives actively, and motor 2 follows. The RHDA output shaft turns about 10 with a speed of 1 (°)/s first, and then goes up to 2.5 (°)/s until the yoke is fully deployed with a hard stop. By this way, the excessive torsion spring energy is consumed and all the arrays lock-up is ensured.

The secondary stage deployment time was between 40 s to 50 s with a stable velocity and a reliable lock-up. In previous tests without a damper or a RHDA, the root hinge velocity was uncontrollable. This free deployment took about 23 s. The curves in Fig. 8 represent the yoke displacements with and without the RHDA respectively. The impact forces are affected by many parameters like the stiffness coefficient, but their proportion is steady. The modulus proportional relationship of them is shown in Fig. 8.
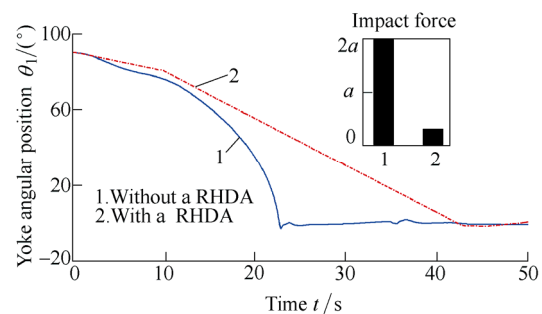


Fig. 8.    Displacement curves comparison

It can be found that the RHDA brings some benefits to the solar array system. With the RHDA, the yoke velocity is controlled smoothly and the impact force drops greatly. It is an effective way to solve the problems that a damper faces.

The root hinge torque was used to validate the established dynamics model. But it is not convenient to measure it directly, since the structure space is limited. However, it can be estimated by the current record of the actuator. In fact, a more accurate measure method is not necessary since huge differences exist between ground conditions and the ideal space environment.

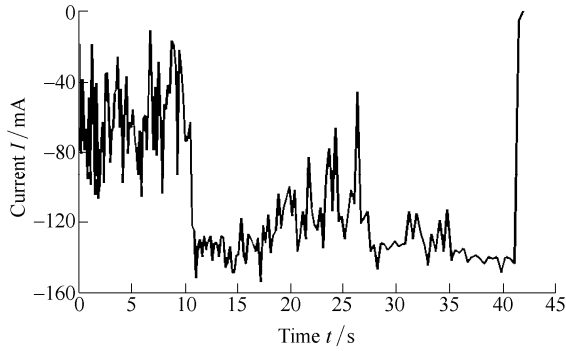Fig. 9 shows an actuator current curve of a certain test.

Fig. 9.　Certain test current curve

The current curve fluctuated heavily, in order to observe the regularity clearly, each sampled current value was averaged with a few former adjacent values. The modified curve is as shown in Fig. 10.
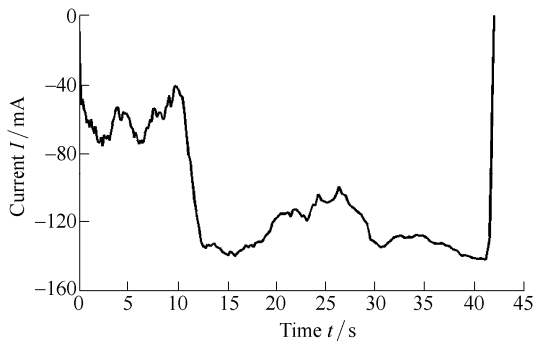


Fig. 10.　Modified current curve

During the deployment, the RHDA probably varied between pushing and pulling the yoke. Though the current direction does not change in Fig. 9(and Fig. 10), it does not mean the torque direction always keeps the same. The RHDA with a high reduction ratio has a large inner resistance, and when an extraneous torque acts as an input for the RHDA, the motor may also do work together to overcome the large friction, so it will not work in an "electric generator" state with a changed current direction."

The motor torque transferred from the armature current is accurate enough, but to get the load of the RHDA output shaft, the reduction ratio and the transmission efficiency of the gear mechanism must be considered. In some relevant researches, factors affecting reduction efficiency were discussed[22]. But it is likely to be different if the reduction ratio is very high.

Normally, a planetary gear unit is converted into an ordinary gear train of identical structure to evaluate its transmission efficiency. A single stage efficiency $\eta_{aH}^{b}$ of the unit is expressed as[23]

$$\eta_{aH}^{b} = 1 - \frac{1 - \eta^{H}}{1 + |i_{ba}^{H}|}, \qquad (10)$$

where $i_{ba}^{H}$ and $\eta^{H}$ are reduction ratio and the transmission

efficiency of the converted form(ordinary gear train), and $\eta^{H}$ is given as

$$\eta^{H} = \eta_{c}^{H} \eta_{z}^{H} \eta_{y}^{H}, \qquad (11)$$

where $\eta_{c}^{H}$, $\eta_{z}^{H}$ and $\eta_{y}^{H}$ denote corresponding efficiencies of gear mesh, bearing loss and oil disturbing loss respectively, and they can be written as

$$\begin{cases} \eta_{c}^{H} = 1 - \sum_{i=1}^{j} f \cdot \mu_{c} \left( \frac{1}{z_{i1}} \pm \frac{1}{z_{i2}} \right), \\ \eta_{z}^{H} = 1 - \frac{\sum_{i=1}^{k} T_{fi} n_{i}}{T_{s} n_{s}}, \\ \eta_{y}^{H} = 1 - \frac{cv^{3/2}}{P}, \end{cases} \qquad (12)$$

where $z_{i1}$ and $z_{i2}$ are tooth numbers of the $i$th gear pair(of $j$ pairs); $f$ and $\mu_{c}$ are constant coefficients about tooth addendum and friction; "+" is for external engaged gear and "−" is for internal engaged gear; $T_{fi}$ and $T_{s}$ are the $i$th bearing friction torque and torque of the driven shaft; $k$ is the number of bearings; $n_{i}$ and $n_{s}$ are rotational speeds of the $i$th bearing and the driven shaft; $c$ is a constant about unit conversion and gear contact area with oil; $v$ is linear speed of the gear, and $P$ is the input power.

For the planetary gear unit used in this paper, the proportions of these velocities and forces are determined, so $\eta_{c}^{H}$ and $\eta_{z}^{H}$ can be seen as constants. According to the relationship among the output torque, the gear linear velocity and the input power, $\eta_{y}^{H}$ can be written as a function of the planetary gear unit output velocity $\dot{\theta}_{1}'$ and the load torque $\tau_{A}'$, and $\eta_{aH}^{b}$ is expressed as

$$\eta_{aH}^{b} = g\left( -\frac{\sqrt{|\dot{\theta}_{1}'|}}{|\tau_{A}'|} \right), \qquad (13)$$

where let function $g(a)$ be a polynomial of high degrees on $a$. In other words, the efficiency can be expressed as an approximation by a polynomial function of high degrees about the independent variable in Eq. (13).

The efficiency of the RHDA reduction mechanism can be seen as a product of efficiencies of the gear stages. The reduction mechanism was tested as follows.

Let the RHDA output shaft rotate with a stable speed in a certain direction, and the speed was set to a group of values from 0.1 (°)/s to 2.5 (°)/s. At each speed, a group of torque values were exerted on the shaft in both directions. The values varied from 0 N • m to 30 N • m.

As stated above, an external torque does work on the RHDA and maybe on the actuators when it has the same direction as the output speed. However, to analyze it conveniently, a so-called efficiency is still calculated just

by Eq. (10), and the result can be called pseudo-efficiency (a negative numerical value). Fig. 11(a) shows the relationship of the RHDA transmission efficiency and its load and speed; Fig. 11(b) includes the pseudo-efficiency. The grid points are the test sampling values. The torque symbol "+" means it does work on the RHDA, while "−" is direct opposite.
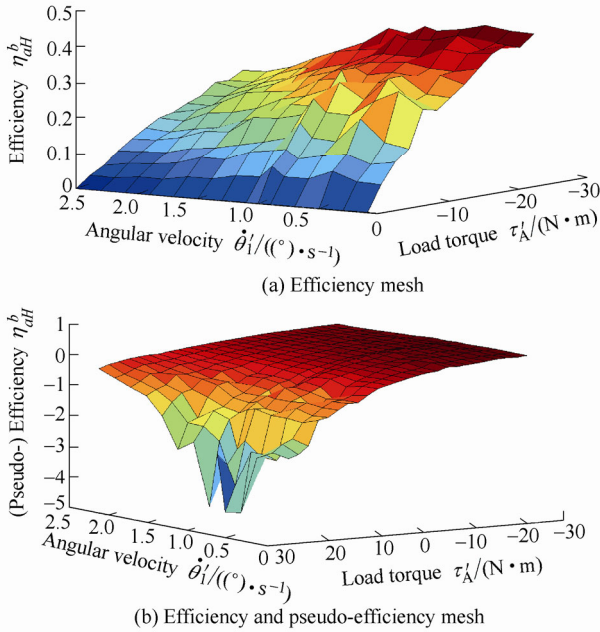


(a) Efficiency mesh



(b) Efficiency and pseudo-efficiency mesh

Fig. 11. Transmission (pseudo-) efficiency mesh

In Fig. 12, the points mark the sampling efficiency values when the load is −18 N • m, which means, they are the points where the mesh in Fig. 11(b) meets the plane $\tau_A' = -18$ N • m; In Fig. 13, the points mark the sampling (pseudo-) efficiency values when the speed is 2.5 (°)/s, which means, they are the points where the mesh in Fig. 11(b) meets the plane $\left| \dot{\theta}_1' \right| = 2.5$ (°)/s. At this speed, the sampling current value varying with load is plotted in Fig. 14.
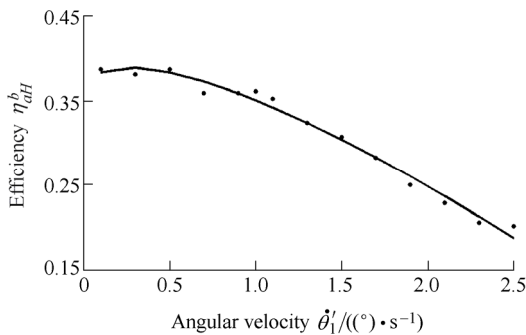


Fig. 12. Relationship between speed and efficiency

As shown in the above figures, the efficiency increases with the increasing of the load modulus, decreases with the increasing of the speed modulus, and it corresponds to the form of Eq. (13). So these parameters are required to introduce to get a more accurate efficiency. Fig. 14 shows a one-to-one correspondence between the load and the current, which means the output torque can be obtained by the current information. The planetary gear unit is a multiple stages structure, so the expression of its efficiency will contain high power item of the independent variable in Eq. (13). However, the power order will not keep increasing as the gear stage increases, or the fitting curve will fluctuate heavily. The data fitting is accurate enough with a cubic or a quartic curve of Eq. (13), as shown in Fig. 12 and Fig. 13. As the torque item is the denominator of the independent variable, the fitting curve in Fig. 13 is divided into two parts by taking zero payloads as a boundary. The stated calibration method is also suitable for analysis of other large reduction ratio gear mechanisms.



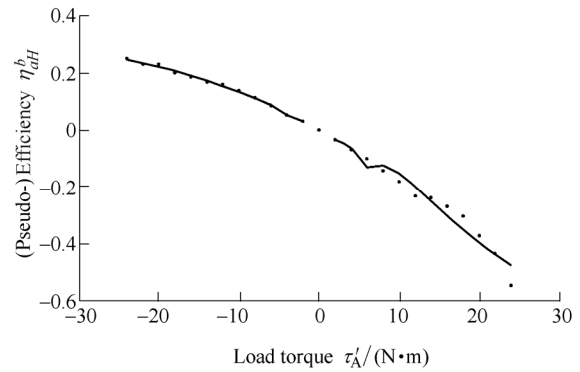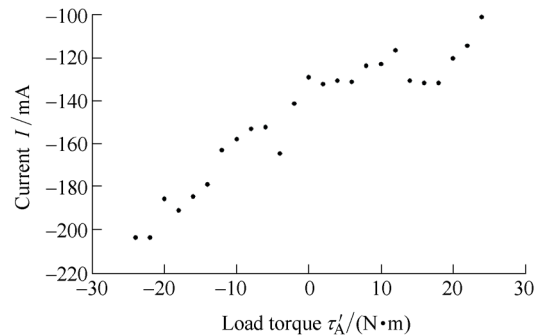Fig. 13. Relationship between load and (pseudo-) efficiency



Fig. 14. Relationship between current and load

The test root hinge drive torque was obtained according to the motor torque and the RHDA efficiency. After being treated the way of Fig. 10, the theoretical evaluation result is compared with the test data in Fig. 15 (with the same frames in Fig. 2).
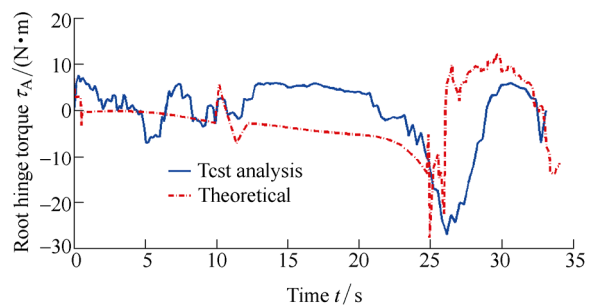


Fig. 15. Comparison of root hinge torque curves

In Fig. 15, the torque curve of the test analysis is shown in solid line, and the theoretical torque curve is shown in dot-dashed line which has a same trend as the solid curve. During the tests, the connection of the RHDA and the yoke is with clearances, so are with the gear pairs, and it is the reason for the differences between the two curves when the velocity rises from 1 (°)/s to 2.5 (°)/s. Affected by the collision algorithms, the calculation results have some deviations from the test analysis values (oscillation due to more than one panel lock-up after 35 s is omitted). Actually, the effect of the impact force on the motor currents is greatly reduced by the large resistance in the reduction mechanism, so the collision algorithm used in Fig. 3 should be refined. However, the results computed from the presented model have a correct trend and predict the maximum value well, which fulfill the requirements of the RHDA components selection completely.

In the tests, motor failure is also simulated without load to check its effect on the RHDA. In Fig. 16(a), it is a normal RHDA output angular velocity curve. When a failure of a running motor happens, the curves of angular velocity with and without the redundancy motor design are compared in Fig. 16(b). The curve with a single motor is shown in solid line and the curve with dual motors is shown in dot-dashed line. All speeds are set to the same value and the motor failure signal is given by artificial setting.



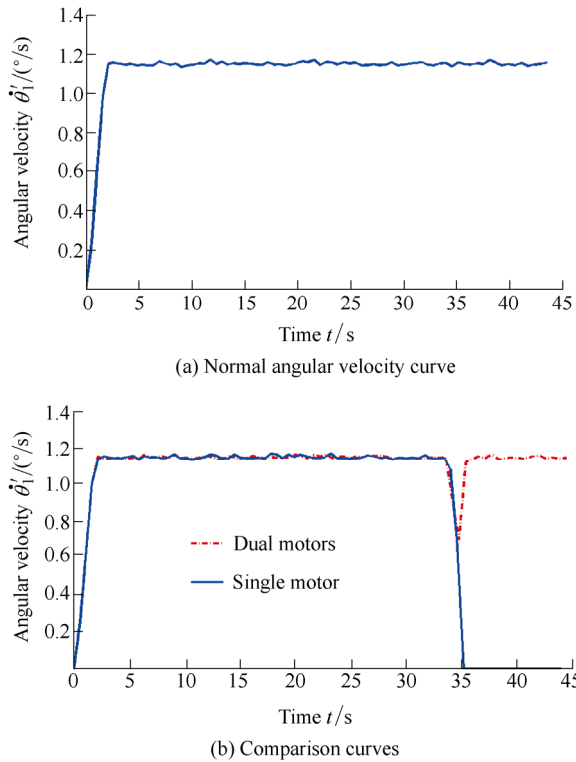(a) Normal angular velocity curve



(b) Comparison curves

Fig. 16.　Output angular velocity curve

It is clear that the redundancy motor can be started automatically as expected if the control cabinet detects the failure signal. So the RHDA with redundancy design has a better tolerance fault capability and a higher reliability.

Furthermore, if the load on the output shaft exceeds the required maximum torque, the torque limiter will disengage and can return to working state by itself after the overload disappears, and this makes further improvements on the reliability of the motor and the gear shafts.

## 5　Conclusions

(1) A multiple degrees of freedom model considering the effects of the drive assembly is formulated, and its dynamics and inverse dynamics coupling problem is solved by the numerical computation method.

(2) A root hinge drive assembly with redundancy characters is developed based on the reliability design methods, and its components selection is performed according to the result computed from the presented model. Ground tests show the drive assembly delayed the deployment time for about 20 s and the yoke lock-up impact force is lower.

(3) The transmission efficiency of the RHDA with a high reduction ratio is studied. The output speed and load are significant factors which affect the efficiency heavily, and the independent variable of the (pseudo-) efficiency function is deduced. Tests are conducted to verify that the efficiency increased with the increasing of the load modulus, and decreased with the increasing of the speed modulus.

(4) According to the reduction efficiency analysis, the RHDA output torque is obtained, and the theoretical result from the established dynamics model is compared with it. It can be concluded that the model is accurate enough for the drive assembly design. Other tests show the reliability of the root hinge drive assembly should be improved with the current design methodologies.

## References

[1] RENSHALL J T, MARKS G. W. The astroEdge* solar array for the NASA small spacecraft technology initiative "Clark" satellite[C]// *Conference Record of the 25th IEEE Photovoltaic Specialists Conference*, Washington, D.C., USA, May 13–17, 1996: 271–276.

[2] ZUCKERMANDEL J W, ENGER S, GUPTA N. Design, build, and testing of TacSat thin film solar arrays[C]//*4th International Energy Conversion Engineering Conference and Exhibit*, San Diego, USA, June 26-29, AIAA Paper, 2006-4198, 2006.

[3] JONES P A, SPENCE B R. Spacecraft solar array technology trends[C]//*Aerospace Conference Proceedings, 1998 IEEE*, Aspen, USA, Mar 21–28, 1998: 141–152.

[4] REN Shouzhi, LIU Liping. Influence of the zero-gravity test facility on the solar array's deployment test[J]. *Spacecraft Engineering*, 2008, 17(6): 73–78. (in Chinese)

[5] MALY J R, PENDLETON S C, SALMANOFF J, et al. Hubble space telescope solar array damper[C]//*Smart Structures and Materials 1999: Passive Damping and Isolation*, Newport Beach, USA, March, 1999: 186–197.

[6] CHENG W L, HILL S, BETENBAUGH T M. Solar array and high gain antenna deployment mechanisms of the STEREO observatory[C]//*AIAA Space 2007 Conference & Exposition*, Long Beach, CA, USA, AIAA Paper, 2007-6096, 2007.

[7] CHO M, NOZAKI Y. Number of arcs estimated on solar array of a geostationary Satellite[J]. *Journal of Spacecraft and Rockets*, 2005, 42(4): 740–748.

[8] PANKOP C A, ALRED J W, BOEDER P A. Mitigation of thruster plume erosion of international space station solar array coatings[J]. *Journal of Spacecraft and Rockets*, 2006, 43(3): 545–550.

[9] ESPINOSA N, HOSEL M, JORGENSEN M, et al. Large scale deployment of polymer solar cells on land, on sea and in the air[J]. *Energy & Environmental Science*, 2014, 7: 855–866.

[10] HWANG E. Seven-panel solar wing deployment and on-orbit maneuvering analyses[C]//*Proc. SPIE, Modeling, Simulation, and Verification of Space-based Systems II*, Bellingham, WA, USA, June, 2005: 48–55.

[11] PORRO J R S, FENILI A. A study about deployment of a solar array on a satellite using DC motors[C]//*17th International Congress of Mechanical Engineering*, Sao Paulo, SP, November, 2003.

[12] LI J L, YAN S Z, GUO F, et al. Effects of damping, friction, gravity, and flexibility on the dynamic performance of a deployable mechanism with clearance[J]. *Proceedings of the Institution of Mechanical Engineers, Part C: Journal of Mechanical Engineering Science*, 2013, 227: 1971–1803.

[13] BAI Z F, ZHAO Y. Attitude motion of spacecraft during oblique solar panel deployment[J]. *Aircraft Engineering and Aerospace Technology*, 2012, 84(2): 109–114.

[14] KWAK M K, HEO S, KIM H B. Dynamics of satellite with deployable rigid solar arrays[J]. *Multibody Syst Dyn*, 2008, 20: 271–286.

[15] SEEGERS B J, GUTHRIE B C, FONTANA R R. Puffin redundant electric propulsion powertrain system[C]//*10th AIAA Aviation Technology, Integration, and Operations Conference*, Fort Worth, TX, USA, AIAA Paper, 2010-9383, 2010.

[16] DING X L, LI X, XU K, et al. Study on the behavior of solar arrays deployment with root hinge drive assembly[J]. *Chinese Journal of Aeronautics*, 2012, 25(2): 276–284.

[17] FIORE J, KRAMER R, LARKIN P, et al. Mechanical design and verification of the TOPEX/Poseidon deployment solar array[C]// *AIAA/ASME/ASCE/AHS/ASC Structures Structural Dynamics, and Materials Conference, 35th*, Hilton Head, SC, USA, AIAA Paper, 94-1323-CP, 1994.

[18] KUMAR P, PELLEGRINO S. Deployment and retraction of cable-driven rigid solar array[J]. *Journal of Spacecraft and Rockets*, 1996, 33(6): 836–842.

[19] CRAIG J J. *Introduction to robotics: mechanics and control*[M]. 3rd ed. New Jersey: Prentice Hall, 2005.

[20] SHIGEHARA M, SHIGEDOMI Y. Multi-body model approach to obtain construction criteria for a large space structure[J]. *Acta Astronautica*, 1997, 41(4–10): 391–400.

[21] ZHOU Zhengfa. *Aerospace reliability engineering*[M]. Beijing: China Aerospace Press, 2006. (in Chinese)

[22] CASTILLO J M. The analytical expression of the efficiency of planetary gear trains[J]. *Mechanism and Machine Theory*, 2002, 37(2): 197–214.

[23] ZHU Xiaolu. *China mechanical design canon* [M]. Vol. 4. Nanchang: Jiangxi Science & Technology Press, 2004: 617–620. (in Chinese)

**Biographical notes**
DING Xilun, born in 1967, is current a professor at *School of Mechanical Engineering and Automation, Beihang University, China*. His research interests include dynamics of compliant mechanisms and robots, design theory of reconfigurable robots, cooperative control of dual redundant manipulators with multi-fingered hand systems, and space robotics.
E-mail: xlding@buaa.edu.cn

LI Xin, born in 1986, is currently a PhD candidate at *School of Mechanical Engineering and Automation, Beihang University, China*. His research interests include space mechanism and redundant drive mechanism.
E-mail: li_xin@me.buaa.edu.cn

# Appendix

$M(\Theta)$ and $V(\Theta,\dot{\Theta})$ can be solved based on the Newton-Euler dynamics algorithm, and they can be expressed as

$$\begin{cases} M(\Theta) = \left( M(i,j) \right)_{4\times4} = \left( M(j,i) \right)_{4\times4}, \\ V(\Theta,\dot{\Theta}) = \left( V(i,j) \right)_{4\times1}. \end{cases}$$

As shown in Fig. 2, we have $l_2 = l_3 = l_4$, so their analytical form can be written as

$$M(1,1) = \sum_{i=1}^{4}\left( I_i + m_i l_1^2 \right) + m_1\left( e_1^2 - l_1^2 \right) +$$
$$\sum_{j=2}^{4}\left( \sum_{i=j}^{4} 2m_i - m_j \right)\cos\left( \sum_{i=2}^{j}\theta_i \right)l_1 l_2 +$$
$$\left[ \sum_{i=2}^{4}\left( i - \frac{7}{4} \right)m_i + \sum_{k=3}^{4}\sum_{j=k}^{4}\left( \sum_{i=j}^{4} 2m_i - m_j \right)\cos\left( \sum_{i=k}^{j}\theta_i \right) \right]l_2^2;$$

$$M(1,2) = \sum_{i=2}^{4} I_i + \sum_{j=2}^{4}\left( \sum_{i=j}^{4} m_i - \frac{1}{2}m_j \right)\cos\left( \sum_{i=2}^{j}\theta_i \right)l_1 l_2 +$$
$$\left[ \sum_{i=2}^{4}\left( i - \frac{7}{4} \right)m_i + \sum_{k=3}^{4}\sum_{j=k}^{4}\left( \sum_{i=j}^{4} 2m_i - m_j \right)\cos\left( \sum_{i=k}^{j}\theta_i \right) \right]l_2^2;$$

$$M(1,3) = \sum_{j=3}^{4}\left( \sum_{i=j}^{4} m_i - \frac{1}{2}m_j \right)\cos\left( \sum_{i=2}^{j}\theta_i \right)l_1 l_2 +$$
$$\left[ \sum_{i=3}^{4}\left( i - \frac{11}{4} \right)m_i + \sum_{j=3}^{4}\left( \sum_{i=j}^{4} m_i - \frac{1}{2}m_j \right)\cos\left( \sum_{i=3}^{j}\theta_i \right) + \right.$$
$$\left. m_4\cos\theta_4 \right]l_2^2 + \sum_{i=3}^{4} I_i;$$

$$M(1,4) = \frac{1}{2}m_4 c_{234} l_1 l_2 + m_4\left( \frac{1}{4} + \frac{1}{2}c_{34} + \frac{1}{2}c_4 \right)l_2^2 + I_4;$$

$$M(2,2) = \sum_{i=2}^{4} I_i + \left[ \sum_{i=2}^{4}\left( i - \frac{7}{4} \right)m_i + \right.$$
$$\left. \sum_{k=3}^{4}\sum_{j=k}^{4}\left( \sum_{i=j}^{4} 2m_i - m_j \right)\cos\left( \sum_{i=k}^{j}\theta_i \right) \right]l_2^2;$$

$$M(2,3) = \sum_{i=3}^{4} I_i + \left[ \sum_{i=3}^{4}\left( i - \frac{11}{4} \right)m_i + \right.$$
$$\left. \sum_{j=3}^{4}\left( \sum_{i=j}^{4} m_i - \frac{1}{2}m_j \right)\cos\left( \sum_{i=3}^{j}\theta_i \right) + m_4\cos\theta_4 \right]l_2^2;$$

$$M(2,4) = I_4 + m_4\left( \frac{1}{4} + \frac{1}{2}c_{34} + \frac{1}{2}c_4 \right)l_2^2;$$

$$M(3,3) = \sum_{i=3}^{4} I_i + \left[ \frac{1}{4}m_3 + m_4\left( \frac{5}{4} + c_4 \right) \right]l_2^2;$$

$$M(3,4) = I_4 + m_4\left( \frac{1}{4} + \frac{1}{2}c_4 \right)l_2^2;$$

$$M(4, 4) = I_4 + \frac{1}{4} m_4 l_2^2;$$

$$V(1, 1) = -\sum_{k=2}^{4} \left( \sum_{i=k}^{4} m_i - \frac{1}{2} m_k \right) \left( \sum_{i=1}^{k} \sum_{j=i+1}^{k} 2\dot{\theta}_i \dot{\theta}_j + \sum_{i=2}^{k} \dot{\theta}_i^2 \right) \sin \left( \sum_{i=2}^{k} \theta_i \right) l_1 l_2 - \sum_{l=3}^{4} \sum_{k=l}^{4} \left( \sum_{i=k}^{4} m_i - \frac{1}{2} m_k \right) \left( \sum_{i=l}^{k} \sum_{j=1}^{i-1} 2\dot{\theta}_i \dot{\theta}_j + \sum_{i=l}^{k} \dot{\theta}_i^2 \right) \sin \left( \sum_{i=l}^{k} \theta_i \right) l_2^2;$$

$$V(2, 1) = \sum_{j=2}^{4} \left( \sum_{i=j}^{4} m_i - \frac{1}{2} m_j \right) \dot{\theta}_1^2 \sin \left( \sum_{i=2}^{j} \theta_i \right) l_1 l_2 - \sum_{l=3}^{4} \sum_{k=l}^{4} \left( \sum_{i=k}^{4} m_i - \frac{1}{2} m_k \right) \left( \sum_{i=l}^{k} \sum_{j=1}^{i-1} 2\dot{\theta}_i \dot{\theta}_j + \sum_{i=l}^{k} \dot{\theta}_i^2 \right) \sin \left( \sum_{i=l}^{k} \theta_i \right) l_2^2;$$

$$V(3, 1) = \sum_{j=3}^{4} \left( \sum_{i=j}^{4} m_i - \frac{1}{2} m_j \right) \dot{\theta}_1^2 \sin \left( \sum_{i=2}^{j} \theta_i \right) l_1 l_2 - m_4 \left( \sum_{i=1}^{3} \dot{\theta}_i \dot{\theta}_4 + \frac{1}{2} \dot{\theta}_4^2 \right) \sin \theta_4 l_2^2 + \sum_{k=3}^{4} \left( \sum_{i=k}^{4} m_i - \frac{1}{2} m_k \right) \left( \dot{\theta}_1 + \dot{\theta}_2 \right)^2 \sin \left( \sum_{i=3}^{k} \theta_i \right) l_2^2;$$

$$V(4, 1) = \frac{1}{2} m_4 \dot{\theta}_1^2 \sin \left( \sum_{i=2}^{4} \theta_i \right) l_1 l_2 + \sum_{k=3}^{4} \frac{1}{2} m_4 \left( \sum_{i=1}^{k} \dot{\theta}_i - \dot{\theta}_k \right)^2 \sin \left( \sum_{i=k}^{4} \theta_i \right) l_2^2.$$

$M(\Theta)$ is always invertible, so $M^{-1}(\Theta)$ can be solved from it.